

1 **Supplementary Material**

2 **P-Wave Arrival-Time Tomography of the Middle East using**
3 **ISC-EHB and Waveform Data**

4 **Ebru Bozdağ, Susini Desilva, Guust Nolet, Rıdvan Örsvuran, Rengin Gök,**
5 **Yahya M. Tarabulsi, Ahmed Hosny, Khalid Yousef, Abdullah Mousa**

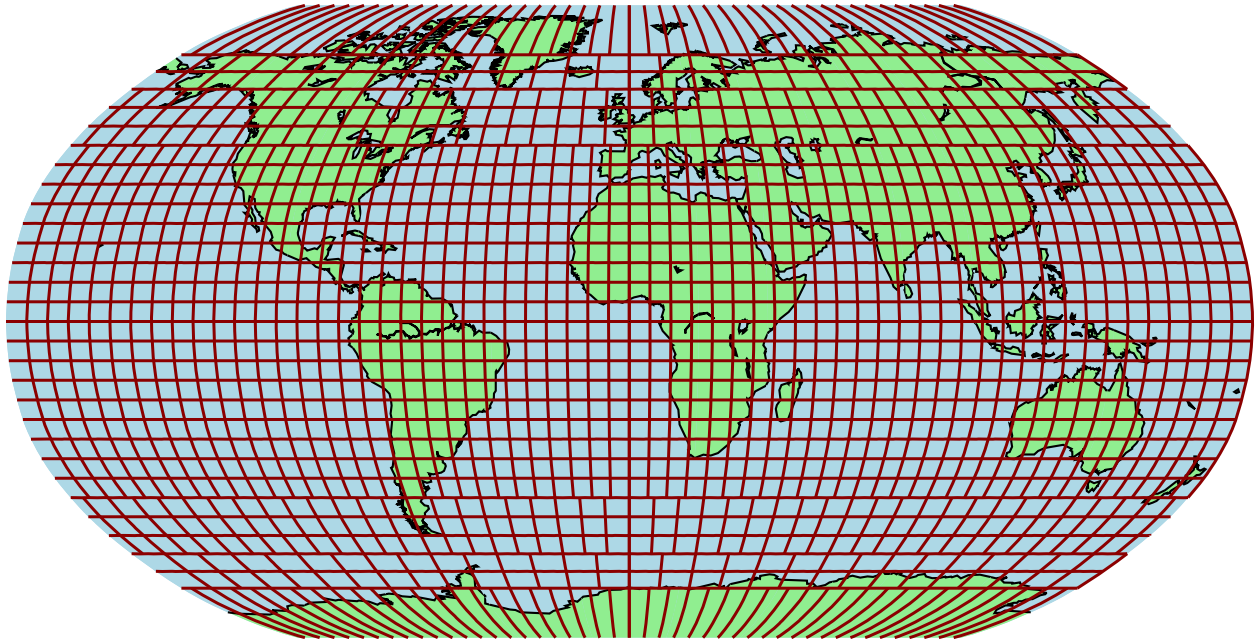


Figure S1 Division of the whole Earth's surface into $1,560 \times 1,560$ lateral event/station regions. This division is applied at three depth levels (< 35 km, < 200 km, and > 200 km), giving possible $3 \times 1,560 \times 1,560$ event-to-station path 'corridors' where a 'corridor' refers to a connection between any two of these $3 \times 1,560 \times 1,560$ blocks.

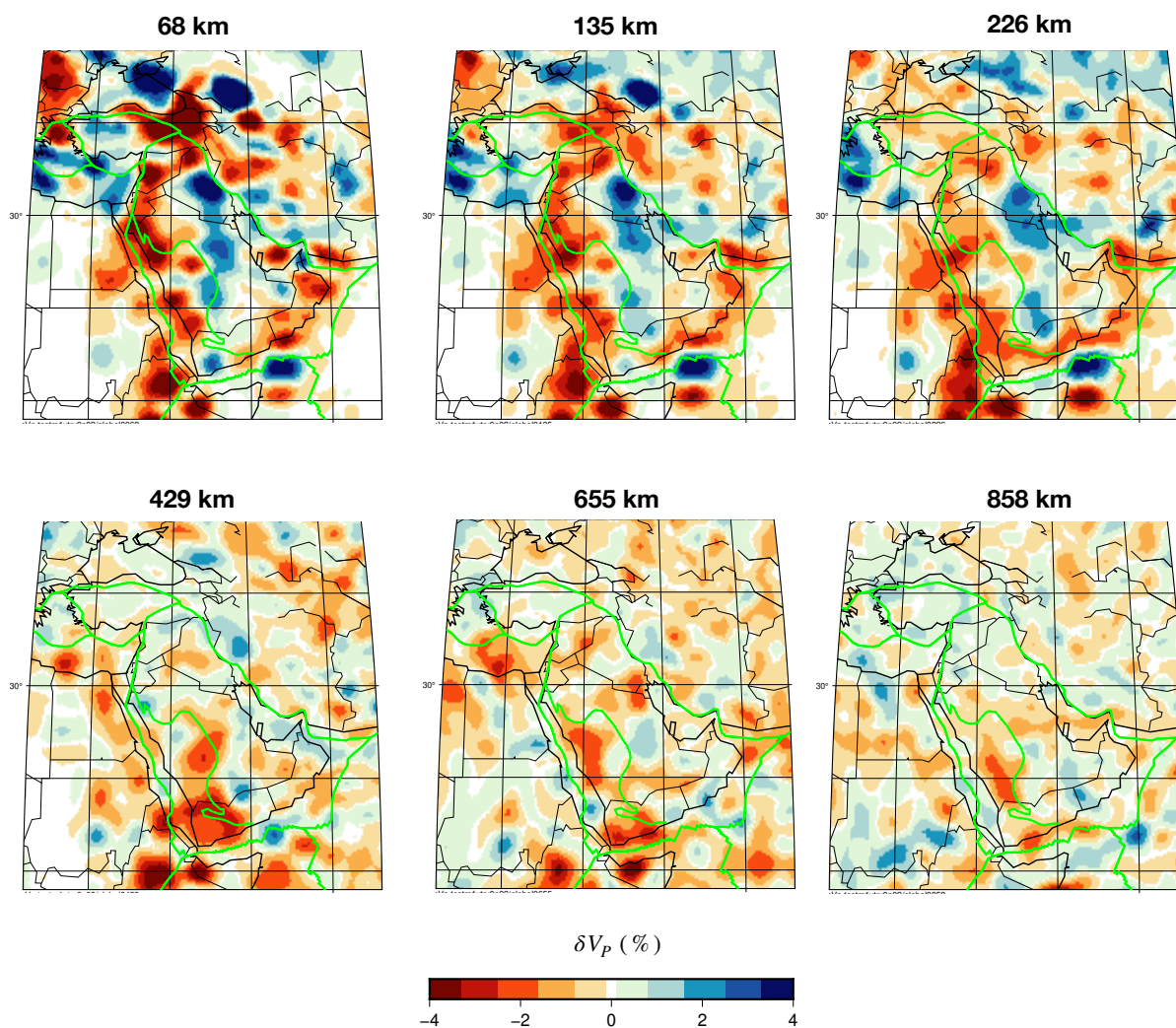


Figure S2 Horizontal cross-sections of P-wavespeed perturbations of the inverted model at various depths with ISC data only. Perturbations are plotted with respect to AK135 (Kennett et al., 1995).

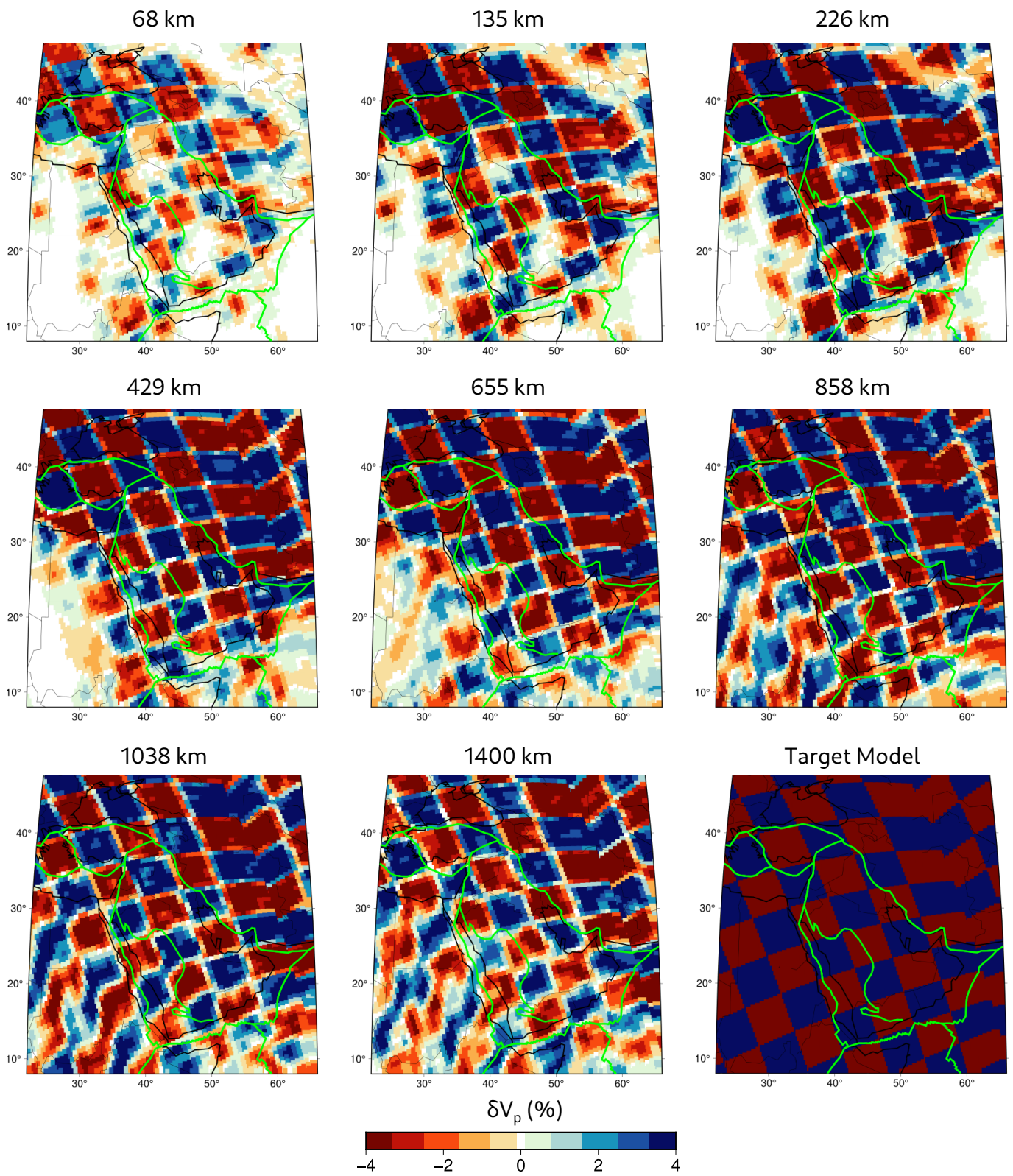


Figure S3 Horizontal cross-sections of the $4^\circ \times 4^\circ$ checkerboard test results for P-wavespeed perturbations at various depths from the ISC data only.

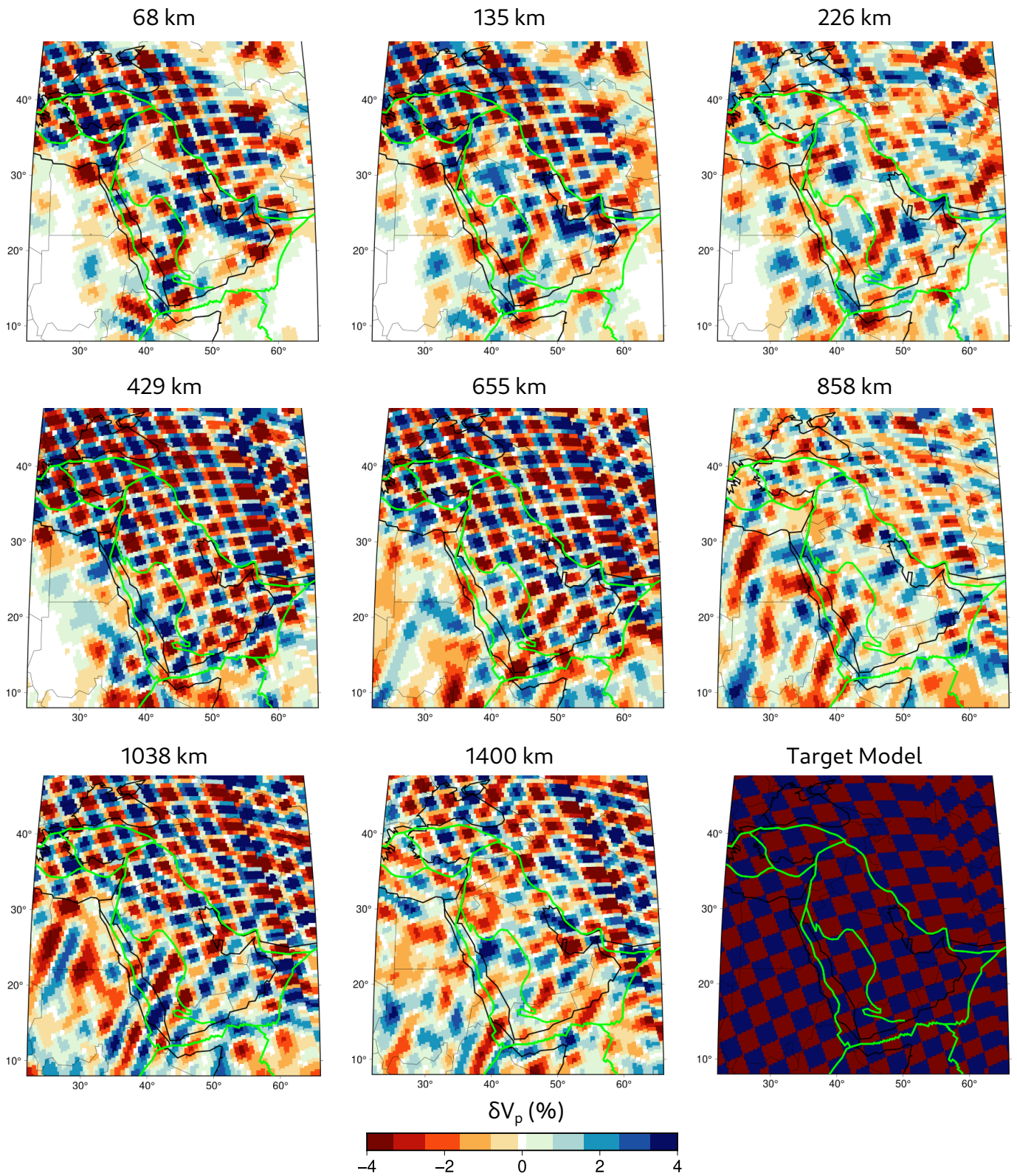


Figure S4 Same as Fig. S3 but for the $2^\circ \times 2^\circ$ checkerboard test results.

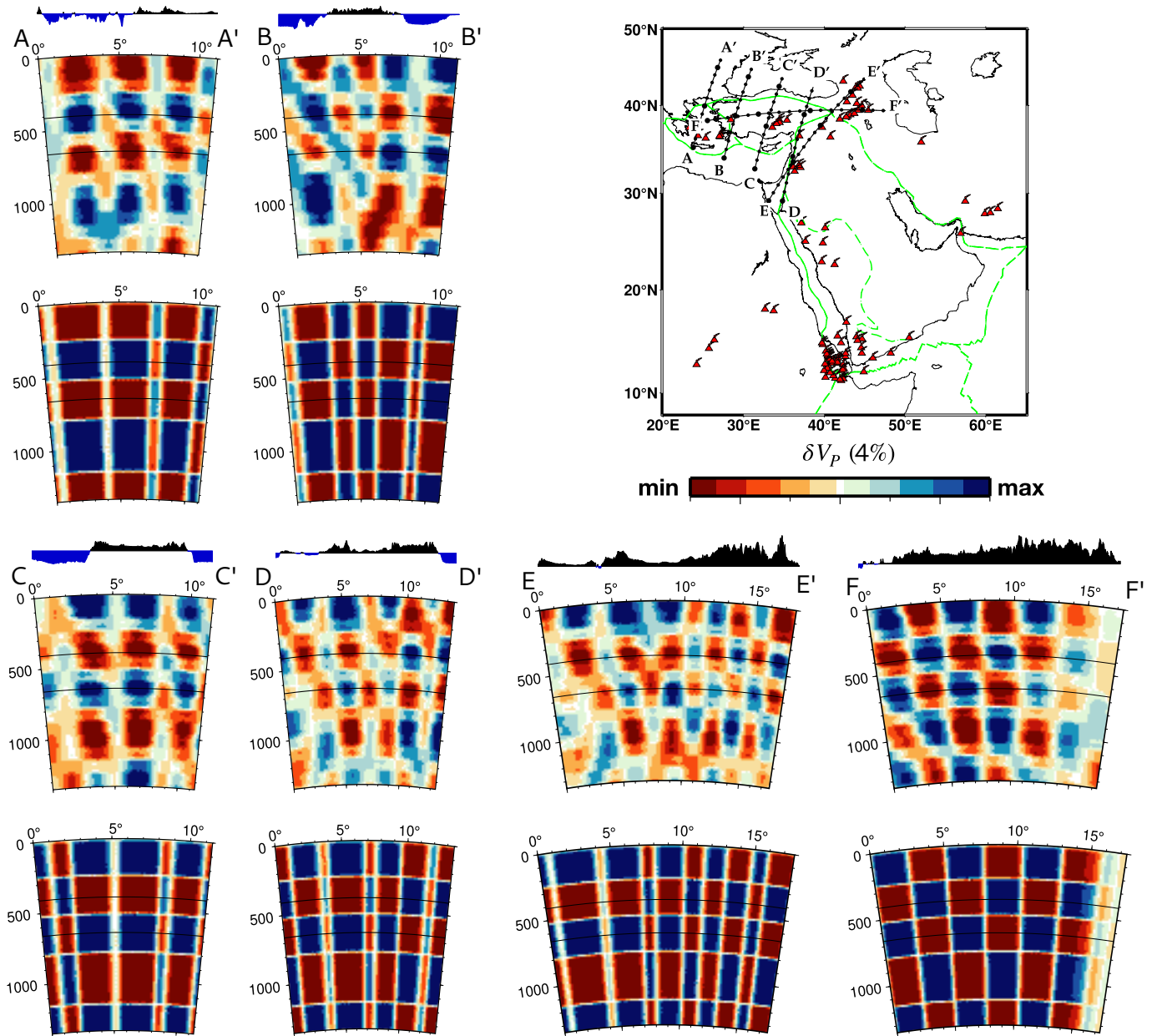


Figure S5 Vertical cross-sections of the $2.4^\circ \times 2.4^\circ$ checkerboard test results shown in Fig. 7 for P-wavespeed perturbations at various depths. ISC data combined with onset-time readings from waveforms recorded by the SGS stations are used during the inversion, and the cross-sections across the Hellenic arc and Anatolia are the same as in Fig. 9. Note that we do not have the regular checkerboard pattern in vertical sections along arbitrary ray paths. The interpolation used to take the cross-sections combined with the applied smoothing cause distortions in the target and inverted checkerboard models.

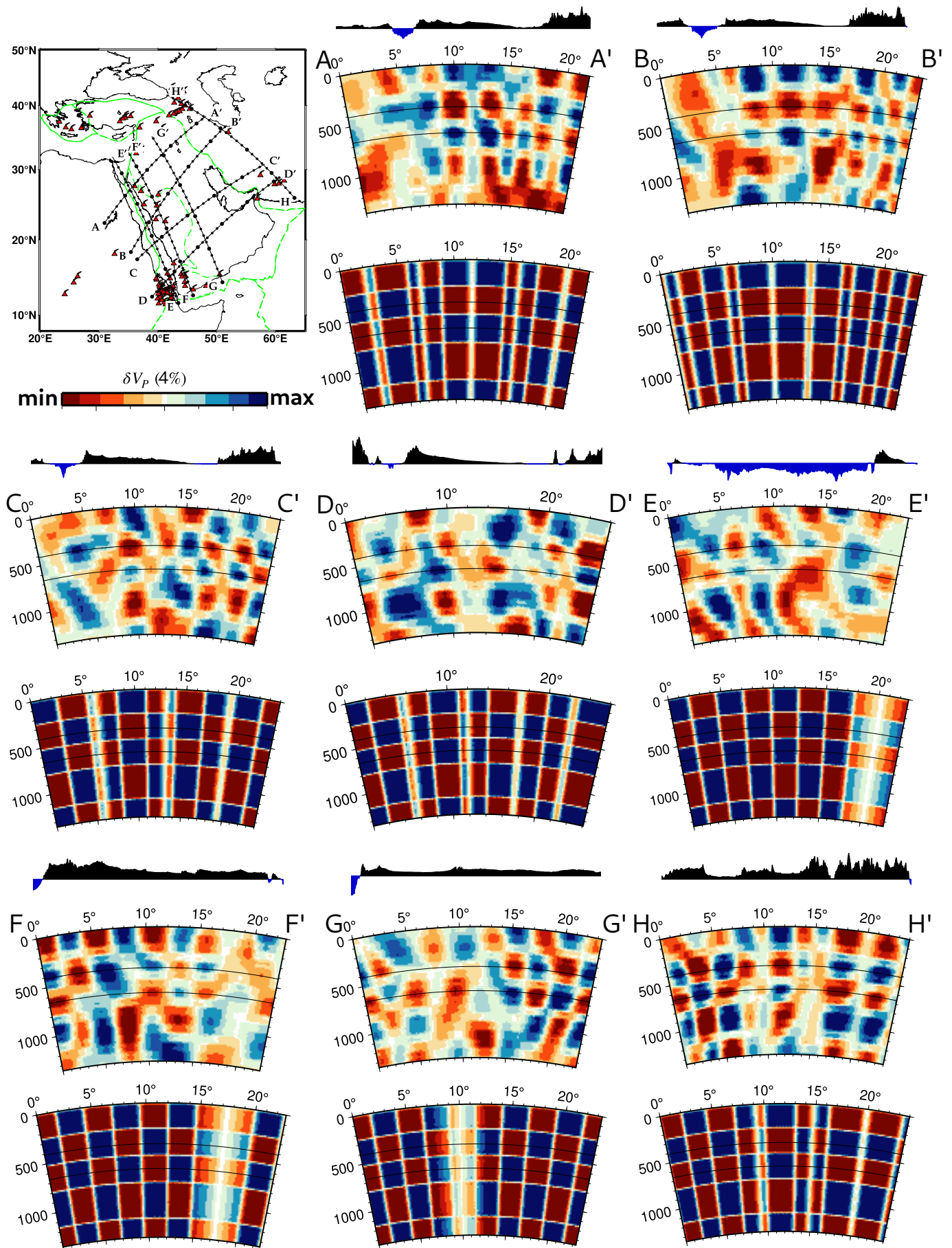


Figure S6 Same as Fig. S5 but for the cross-sections across the Arabian Peninsula shown in Fig. 10.

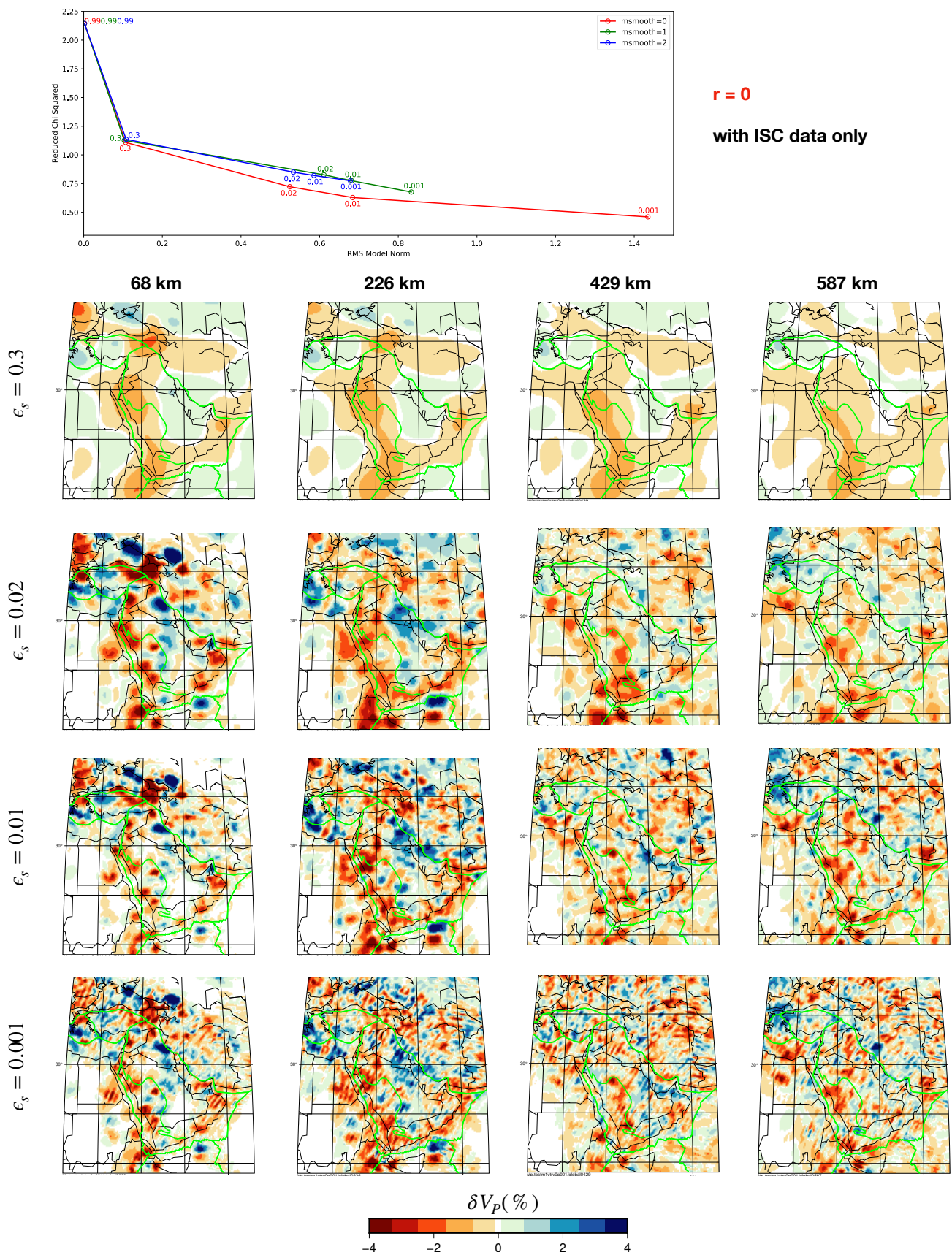


Figure S7 L-curve analysis for the lowest level of smoothing ($r = 0$) using the ISC data only. The cross-sections correspond to different levels of damping.

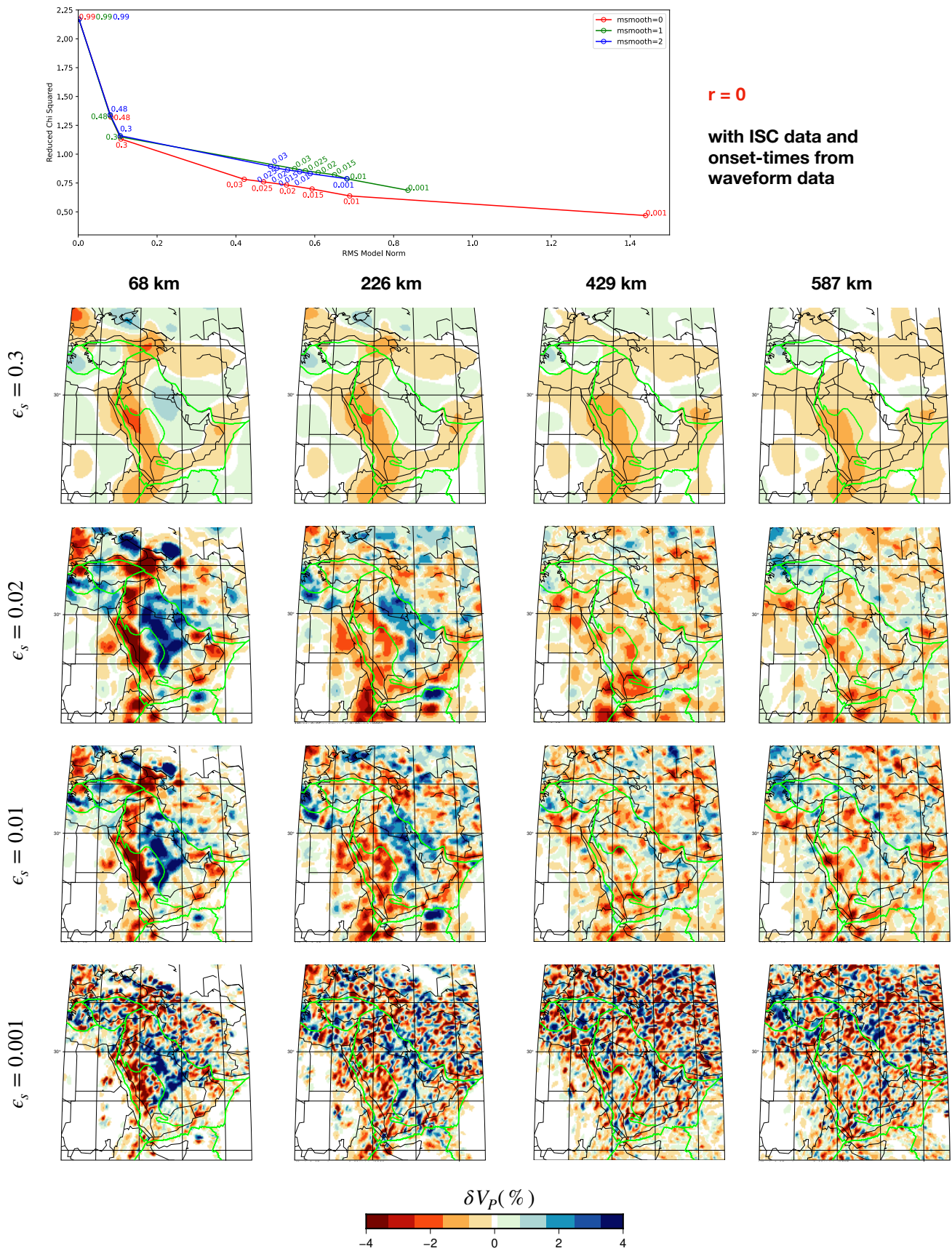


Figure S8 Same as Fig. S7 but for ISC data with onset-time readings from waveform data.

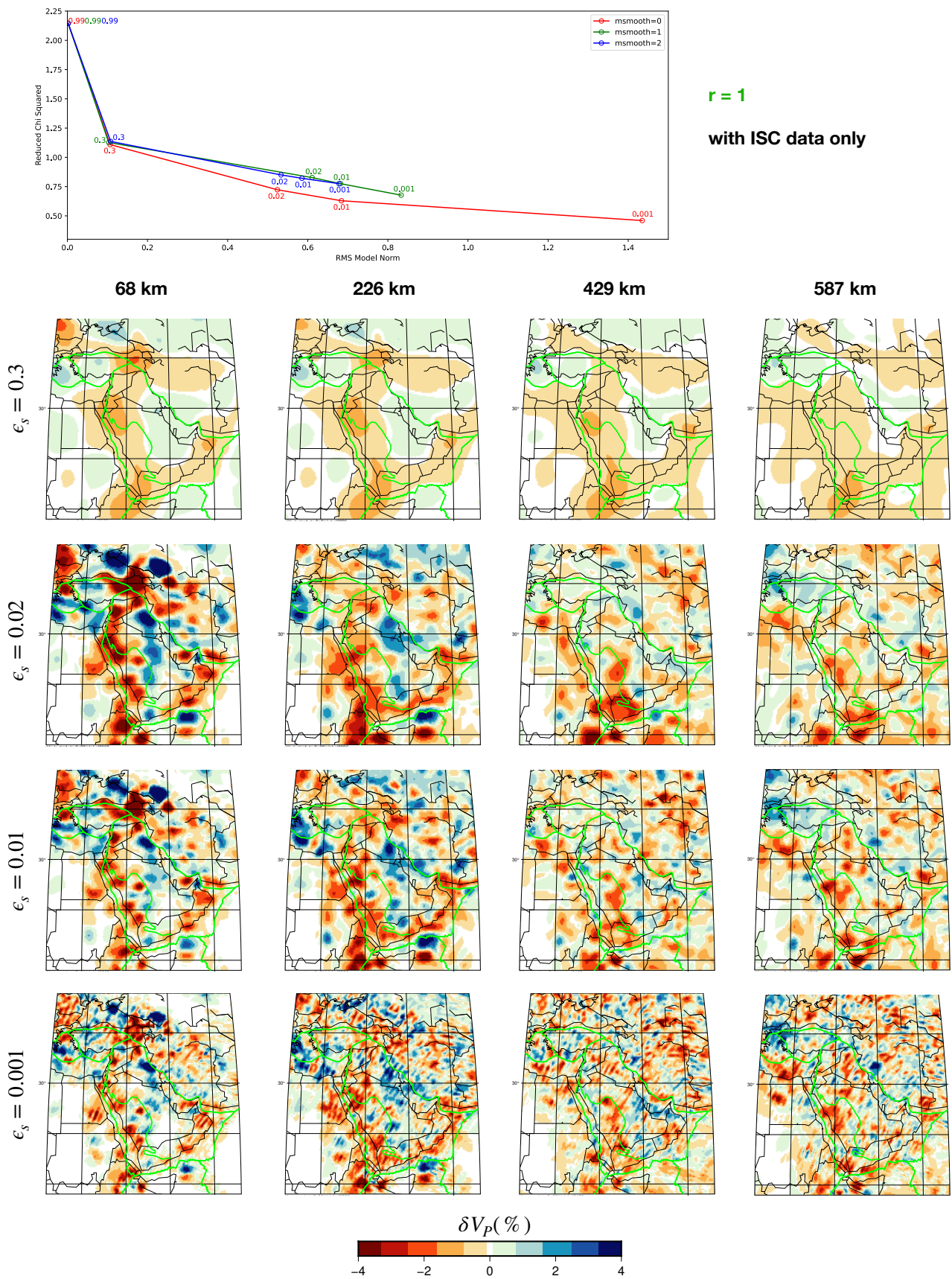


Figure S9 Same as Fig. S7 but for the mid-level of smoothing ($r = 1$).

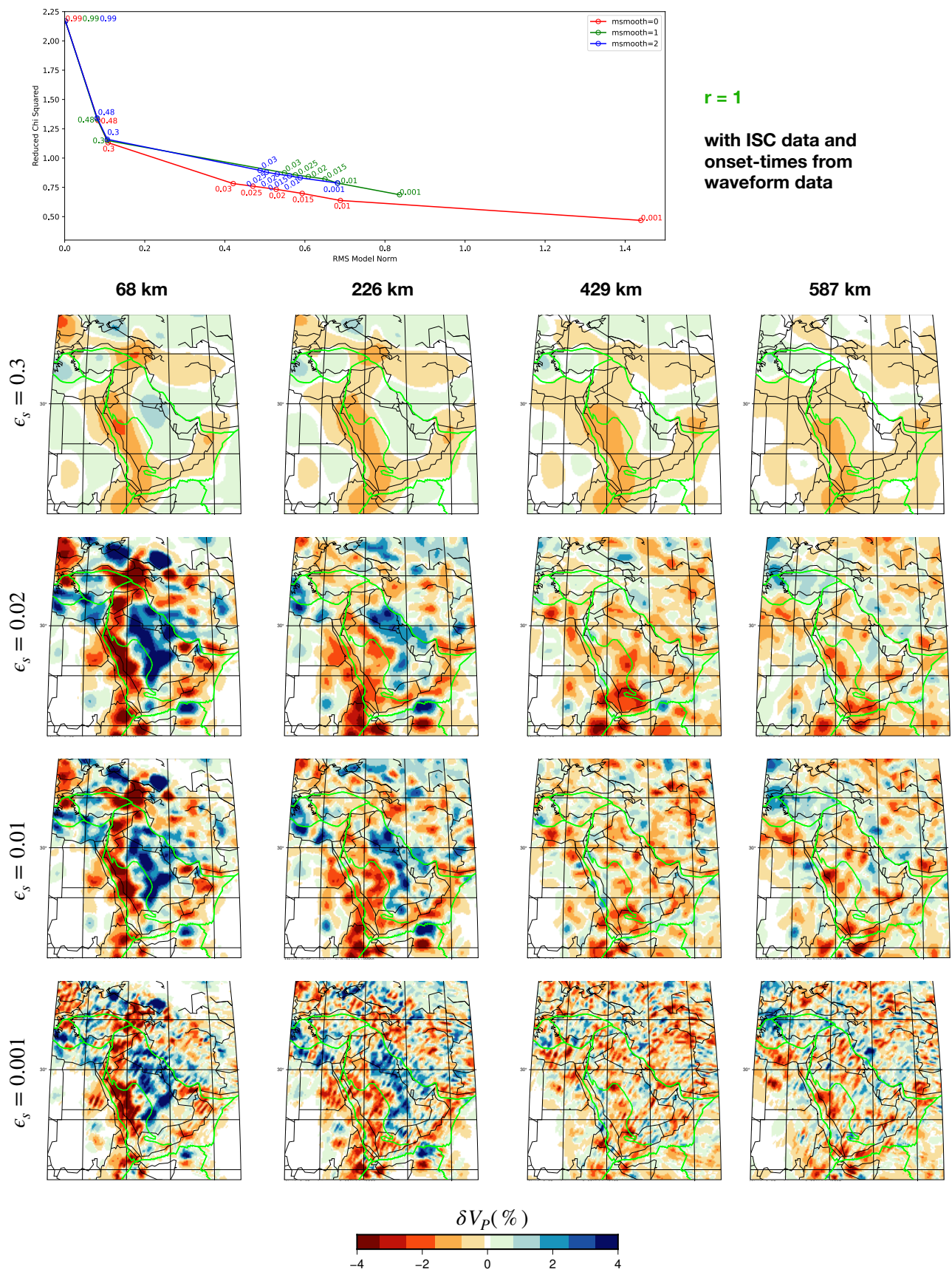


Figure S10 Same as Fig. S9 but for ISC data with onset-time readings from waveform data.

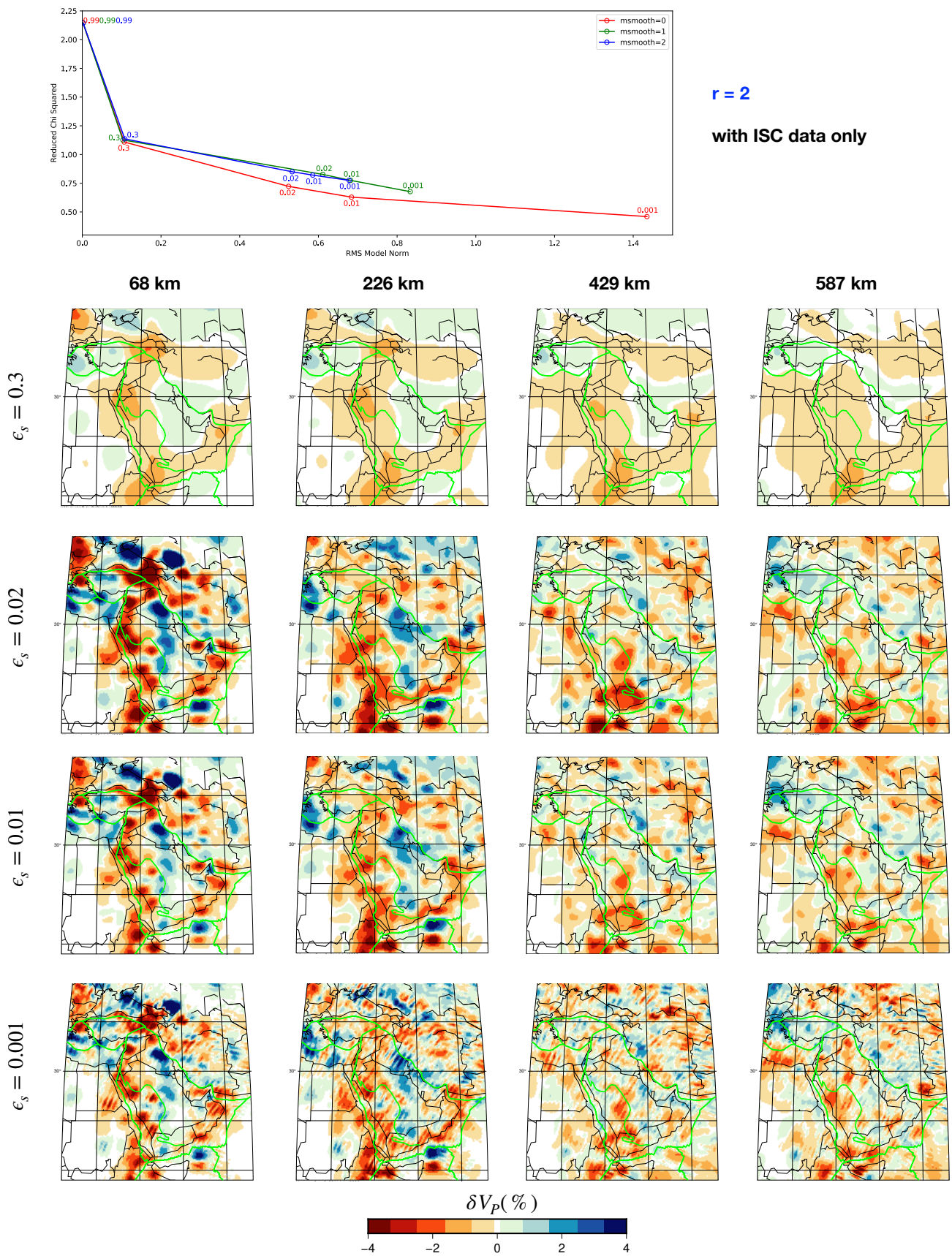


Figure S11 Same as Fig. S7 but for the highest-level of smoothing ($r = 2$).

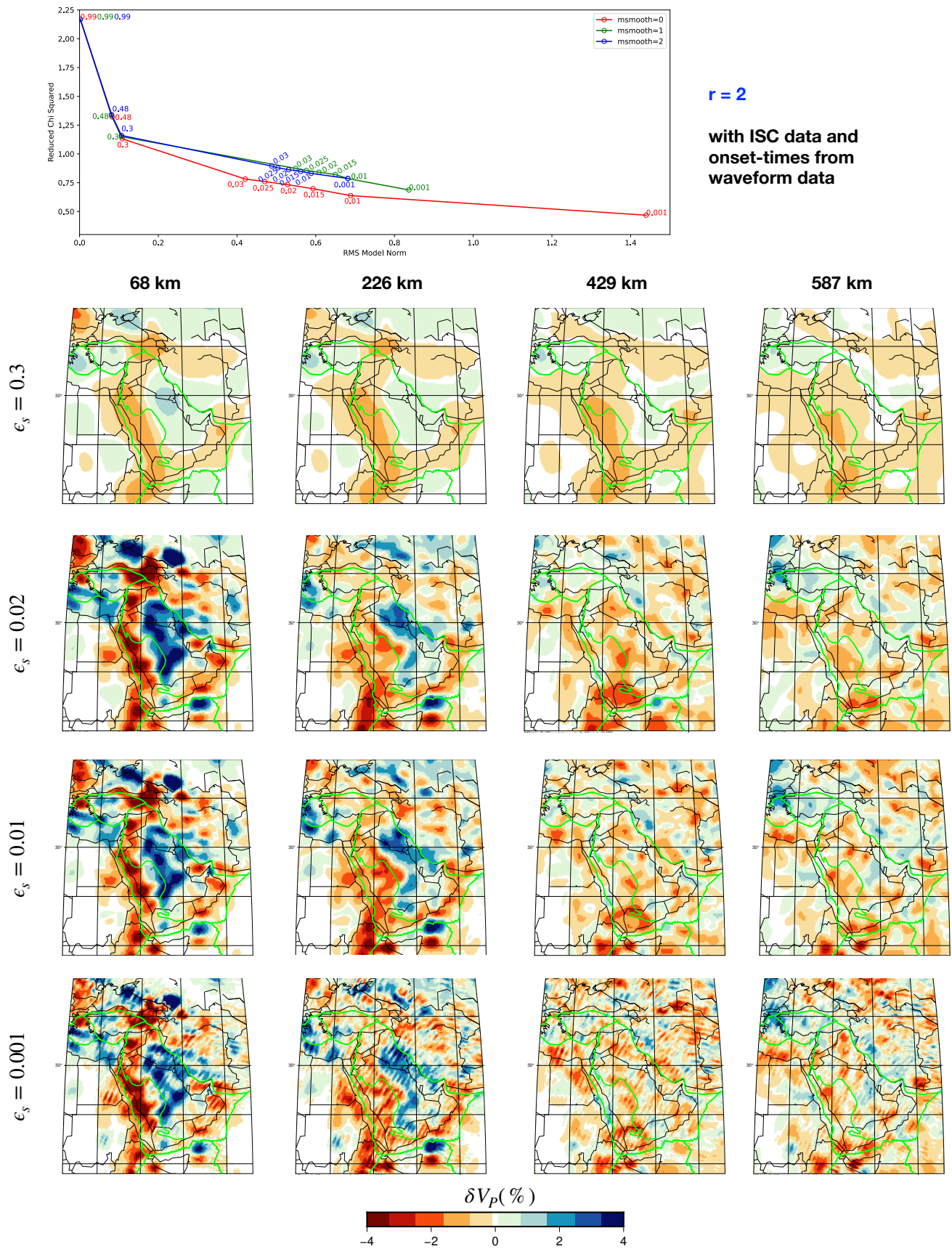


Figure S12 Same as Fig. S11 but for ISC data with onset-time readings from waveform data.

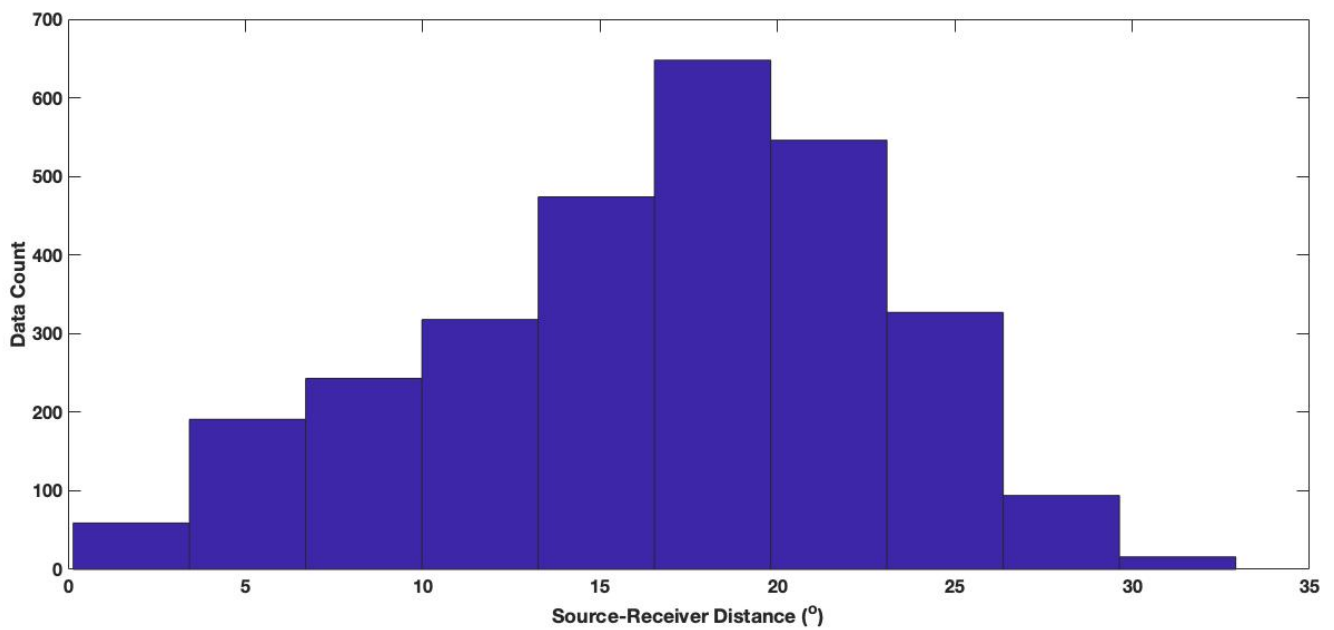


Figure S13 Histogram of epicentral distances for the 2,916 waveforms provided by the Saudi Geological Survey (SGS) from the Arabian Peninsula, which are used to pick P-wave arrival times assimilated in inversions.

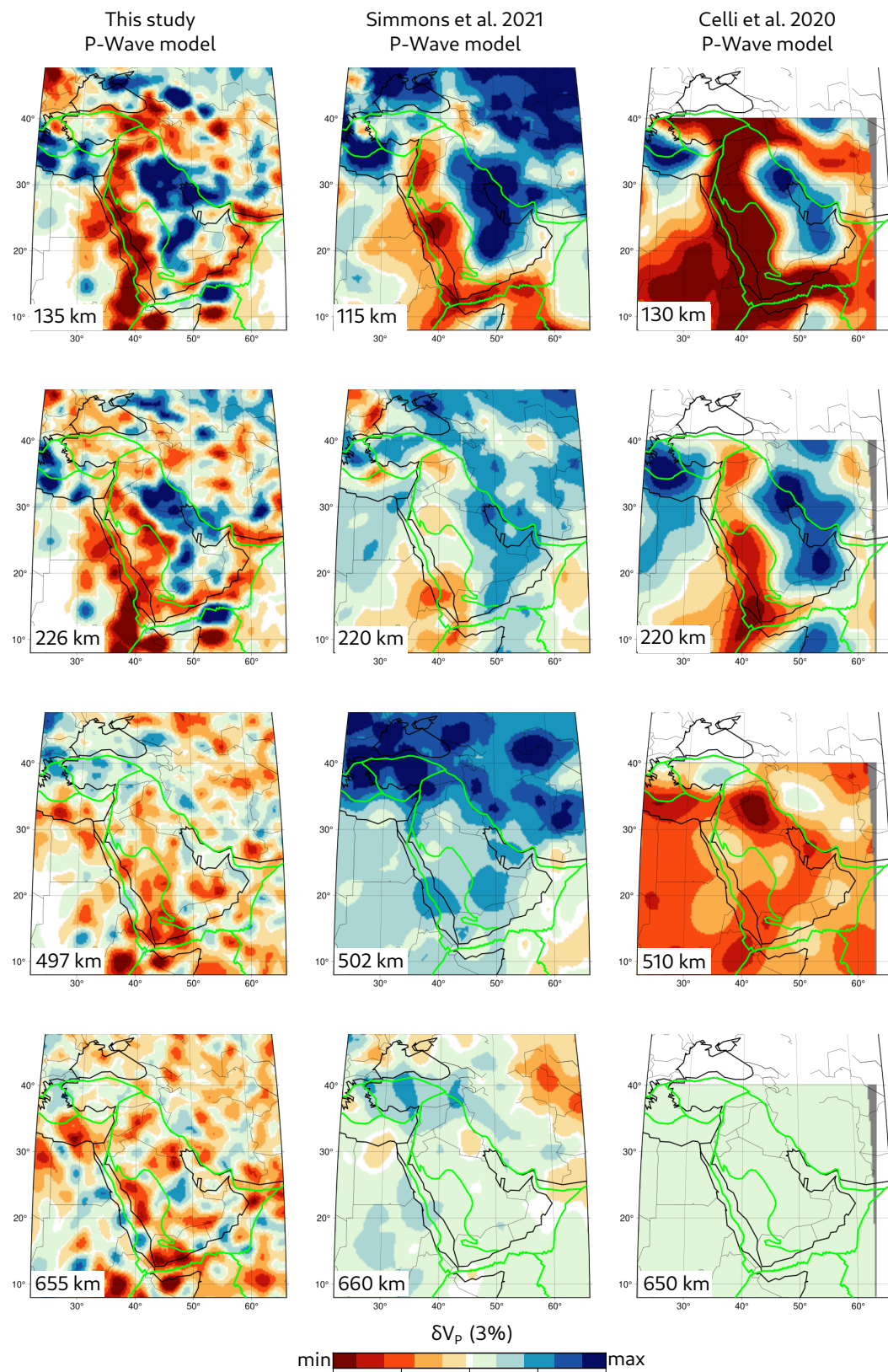


Figure S14 Comparison of horizontal sections of the P-wavespeed models of [Simmons et al. \(2021\)](#) and [Celli et al. \(2020\)](#) to the P-wavespeed model from this study. Perturbations are plotted with respect to AK135.

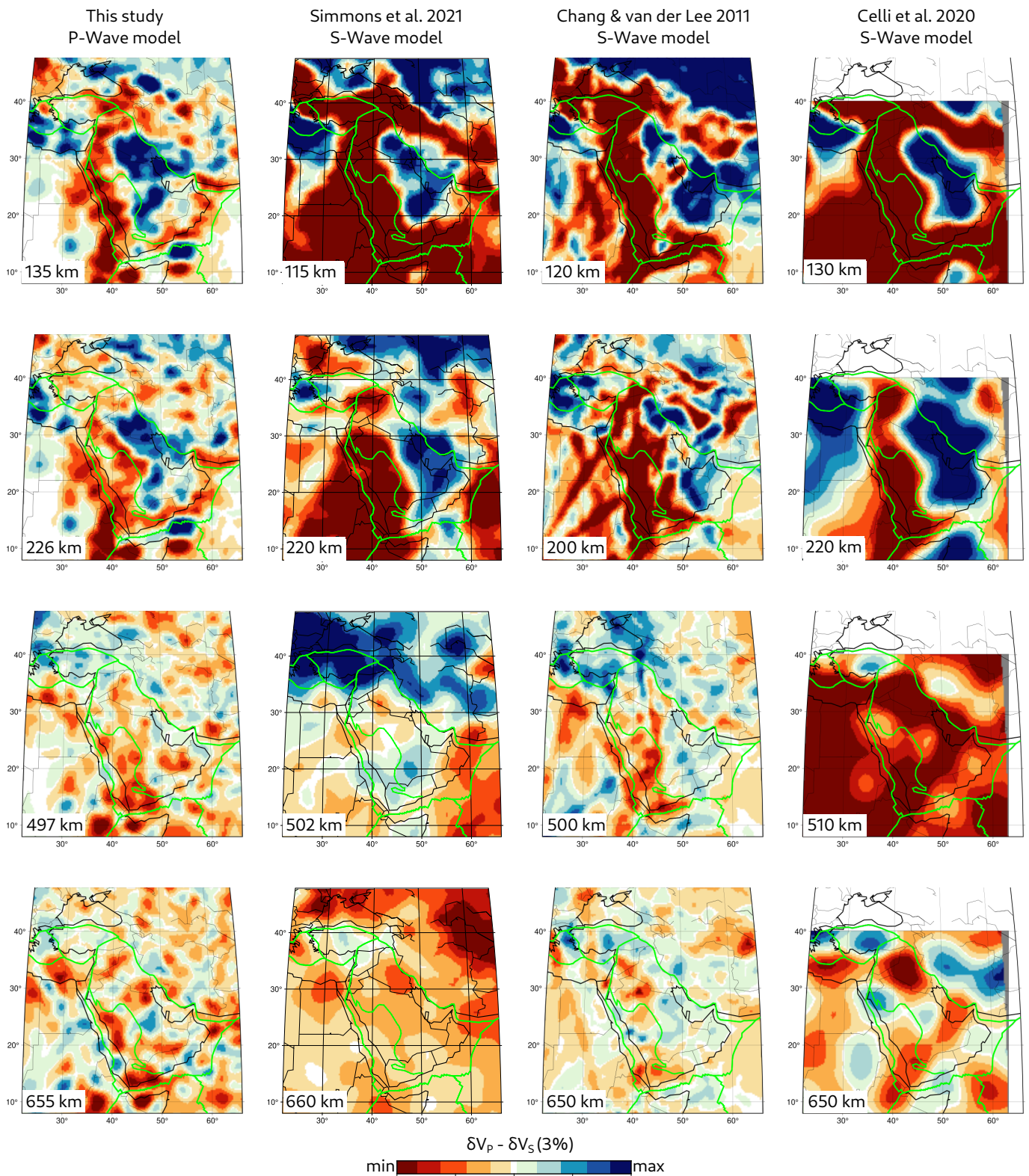


Figure S15 Comparison of the horizontal sections of the S-wavespeed models of Simmons et al. (2021), Chang and Van der Lee (2011), and Celli et al. (2020) to the P-wavespeed model from this study. Perturbations are plotted with respect to AK135.

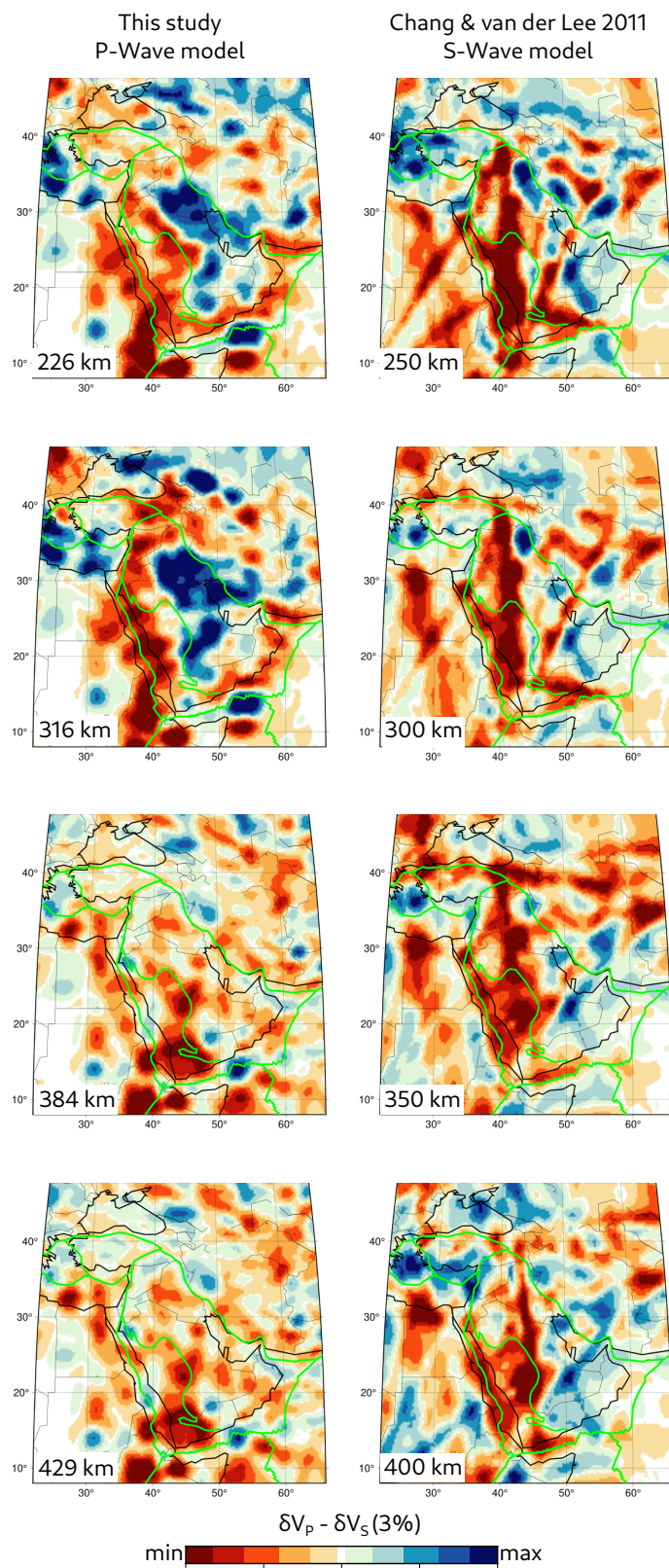


Figure S16 Same as Fig. S15 but comparisons are only with the S-wavespeed model of Chang and Van der Lee (2011) at different depths. Perturbations are plotted with respect to AK135.

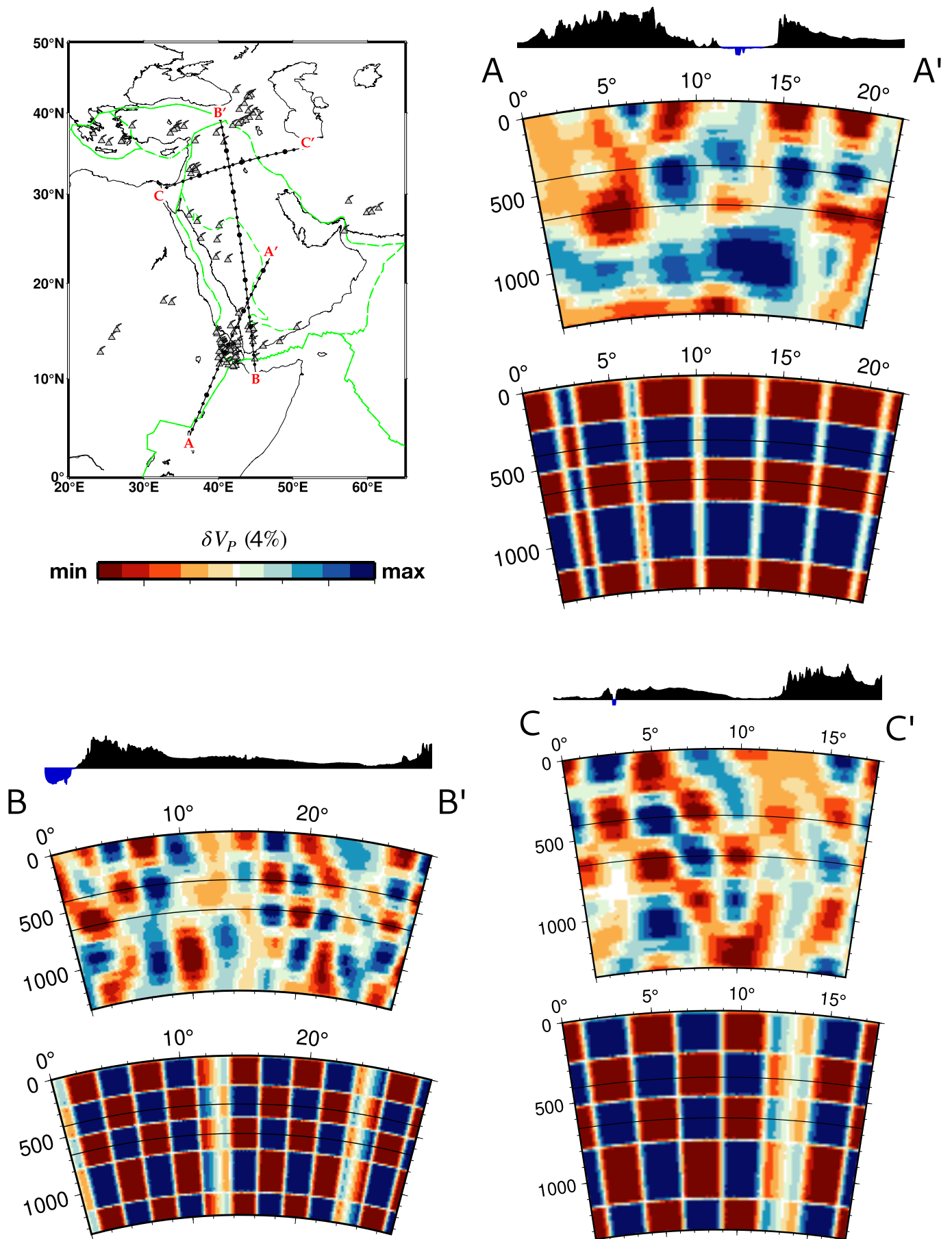


Figure S17 Same as Fig. S5 but for the cross-sections shown in Fig. 12. Note that we do not have the regular checkerboard pattern in vertical sections along arbitrary ray paths. The interpolation used to take the cross-sections combined with the applied smoothing cause distortions in the target and inverted checkerboard models.

6 **References**

- 7 Celli, N., Lebedev, S., Schaeffer, A., and Gaina, C. African cratonic lithosphere carved by mantle plumes. *Nat.*
8 *Commun.*, 11:92, 2020. doi: 10.1038/s41467-019-13871-2.
- 9 Chang, S.-J. and Van der Lee, S. V. Mantle plumes and associated flow beneath Arabia and East Africa. *Earth and*
10 *Planetary Science Letters*, 302(3):448 – 454, 2011. doi: 10.1016/j.epsl.2010.12.050.
- 11 Kennett, B. L., Engdahl, E., and Buland, R. Constraints on seismic velocities in the Earth from traveltimes. *Geo-*
12 *physical Journal International*, 122(1):108–124, 1995. doi: 10.1111/j.1365-246x.1995.tb03540.x.
- 13 Simmons, N. A., Myers, S. C., Morency, C., Chiang, A., and Knapp, D. R. SPiRaL: A Multiresolution Global Tomography
14 Model of Seismic Wave Speeds and Radial Anisotropy Variations in the Crust and Mantle. *Geophysical Journal*
15 *International*, 227(2):1366–1391, Nov. 2021. doi: 10.1093/gji/ggab277.